JOURNAL OF MATERIALS SCIENCE 31 (1996) 1843–1855

Semi-automated image analysis of the true tensile drawing behaviour of polymers to large strains

A. R. HAYNES, P. D. COATES
Interdisciplinary Research Centre for Polymer Science and Technology, Department of Mechanical and Manufacturing Engineering, University of Bradford, Bradford, West Yorkshire BD7 1DP, UK

An image analysis system has been developed using commercially available hardware with custom software to investigate the deformation behaviour of solid polymers in uniaxial tension. This technique provides a rapid, semi-automated non-contacting method for determining true process stress–strain–strain-rate behaviour for both homogeneous and inhomogeneous deformation. The relative displacements of printed transverse grid lines are determined from images captured during a standard monotonic tensile test, providing local measures of strain. The examination of a time series of images allows the generation of true strain-rate data, and concurrent monitoring of the total draw force from the load cell allows the generation of true stress data at those times when the images are captured. Therefore, it is possible to produce a series of process uniaxial true stress–strain curves for individual "elements" of material within the gauge length of the specimen. Synthetic elastomers drawn at ambient temperature have been found to display relatively homogeneous deformation, resulting in a simple process axial stress–strain curve for the single-speed test, whereas in the case of inhomogeneous deformation ("necking") exhibited by polypropylene, it is verified that each element of material experiences a slightly different deformation process. This spatially variant deformation is related to the original location of the particular element with respect to the point of neck initiation.

1. Introduction

Previous studies have shown that it is possible to draw various polymers under conditions that produce very high draw ratios, and correspondingly highly aligned structures with values of Young's modulus approaching the theoretical maximum [1–4]. However, the many potential benefits that polymers can offer are not always fully exploited commercially due to the lack of established and proven design analysis techniques [5]. Commercial scale tensile drawing processes have been successfully established to reproduce these oriented structures in order to make use of the enhanced properties [6], but prototyping is often the only effective way to test the suitability of a design – a costly and time-consuming exercise.

Testing polymers to produce comprehensive true stress–strain–strain-rate data requires considerable effort due to the different material responses that may be observed under different experimental conditions. Also, the inherent difficulty of maintaining homogeneous deformation at high strains causes problems, because immediately the material begins to neck, the engineering stress becomes a poor approximation of the true stress. The lack of consistent and comprehensive sets of true stress–strain data for polymers has hampered the development of constitutive models for this type of deformation, and led to a number of UK initiatives involving the acquisition and presentation of this kind of data [7].

Furthermore, the increasing demand for accurate material stress–strain constitutive relations for use in modelling studies has led to the need for accurate data to be obtained from tensile test specimens *in situ*. Established numerical techniques, such as finite element analysis (FEA), can only produce valid simulations where accurate material property data are available.

In the current work, a semi-automated image analysis technique is used to quantify the surface strains experienced by a tensile specimen by measuring dimensions from a printed grid. Local true stress may then be calculated to a good approximation using the assumption of deformation at constant volume. The true stress-strain data generated from these tests may then be used to develop further understanding of deformation processes (including the molecular level) and in the formulation and validation of constitutive equations. Although the current work has dealt solely with the uniaxial deformation of specimens in a simple tensile test, the strain measurement technique is, in principle, equally valid in the study of biaxial deformation, and preliminary studies appear encouraging.

A review of the various methods available to generate true stress data for polymer specimens was given by Haward [8], who concluded that the method of

0022–2461

G'Sell and Jonas [9], where a linear transducer is used with hourglass shaped specimens to measure the minimum diameter of the specimen, was the most applicable method. This technique has since been refined to use image analysis to provide a non-contacting measure of the minimum diameter and the local radius of curvature to determine true stress and strain [10]. Strain data can be fed back to the servo-hydraulic tester to achieve testing at constant true strain rate, but at limited strain and strain rates. In the work reported here, tests are not undertaken at constant strain rate but constant cross-head speed, so the system simply observes the behaviour of specimens in the normal tensile test using an automated grid method. Following the definition given by Sirkis and Lim [11], automated grid methods are defined as "those methods using solid state technology for direct measurement of relative motion of grid spots or lines". Although much work has been published on the use of automated grid methods to measure the small strains occurring in metals undergoing tensile and compressive deformation [11–18], little has been published on the automated grid method applied to polymers, where the strains are much higher and cause distortion of the marked grid [19–21]. Also, as deformation is expected to be inhomogeneous for many polymers, it is not possible to average out many measurements across or along the gauge length of the specimen to improve the results by reducing noise, because variations in strain are expected. Work has been published containing results generated by manually measuring deformation in polymer specimens from photographs taken during testing, at both high [22–24] and low [25] strains.

A brief description of image analysis studies for polymer deformation in our laboratories has been given by Coates *et al.* [20] in the context of in-process measurements on polymers. In the current work, dumb-bell shaped specimens are marked with a contrasting regular grid (1/16 in ($\sim$0.16 cm) line pitch) using a simple silk-screen printing process.

2. Equipment and instrumentation

A block diagram of the measuring system is presented as Fig. 1. The system operates on an IBM PC compatible DOS platform and comprises a Data Translation DT2861 frame grabber with a DT2878 array processor, a DT2835 combined analogue to digital conversion and timer board, a Pulnix TM-765 area scan CCD camera, and an Instron 1026 bench-top tensile tester fitted with a purpose-built high air flow oven, providing control of both temperature and surface heat transfer [20, 21].

The frame grabber allows the capture and storage of up to 16 512 × 512 × 8 bit grey level frames at speeds up to the interlaced CCIR maximum (25 Hz) frame rate. An external electronic trigger is taken from the Instron at the start of the test to synchronize all data acquisition to a reference time. Subsequent images and load data are captured at regular intervals under the control of the timing facility of the DT2835. All software has been written in the C programming language.

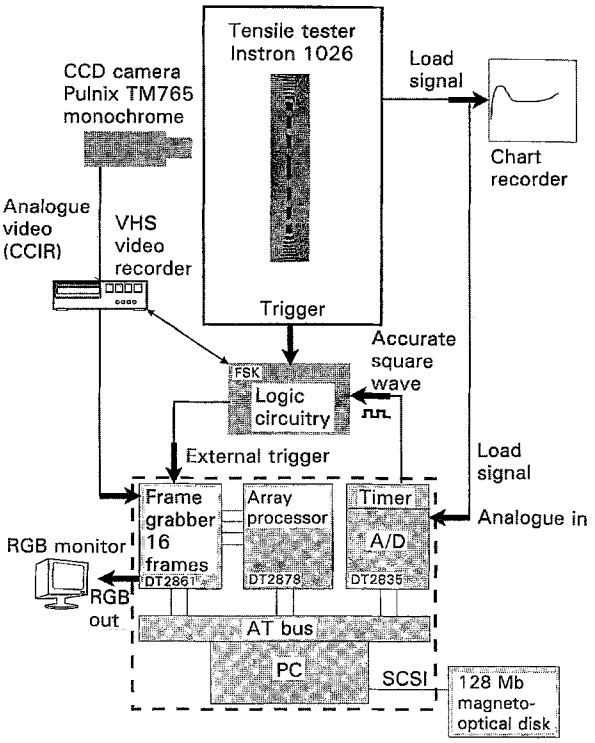

Figure 1 Image analysis equipment block diagram.

Hardware limitations on memory often restrict automated grid methods to two images taken before and after deformation. The frame grabber used in the current work was chosen for its ability to capture 16 images in on-board memory, so that more detailed strain–time data could be generated. Also, it is possible to record the images from the camera on a standard VHS video recorder, where they may be stored and analysed later. When re-analysing a pre-recorded test, accurate synchronization is obtained using custom electronics designed to create a trigger to signal to the software when the test started. This technique allows a single test to be re-sampled at a range of image capture rates, such that in the study of inhomogeneous deformation it is possible to capture 16 images in rapid succession during the early neck-formation period of the test, then re-sample the video at a slower sampling rate to study the neck propagation. Synchronization is achieved by a frequency shift keying (FSK) technique, where the two logic states of the trigger are represented by two frequencies that can be recorded on to the audio channel of the video tape. When the test starts, the frequency of the tone is changed, and this can be detected by the hardware to trigger the acquisition of the images when the video is replayed. Such a facility can clearly allow the capture of information at sites geographically remote from the image analysis PC.

A typical digitized draw load curve for a necking polymer is presented as Fig. 2, and typical images from the test are shown in Fig. 3.

3. Image analysis segmentation method

Image segmentation is the operation of extracting features of interest from a given image. In the current

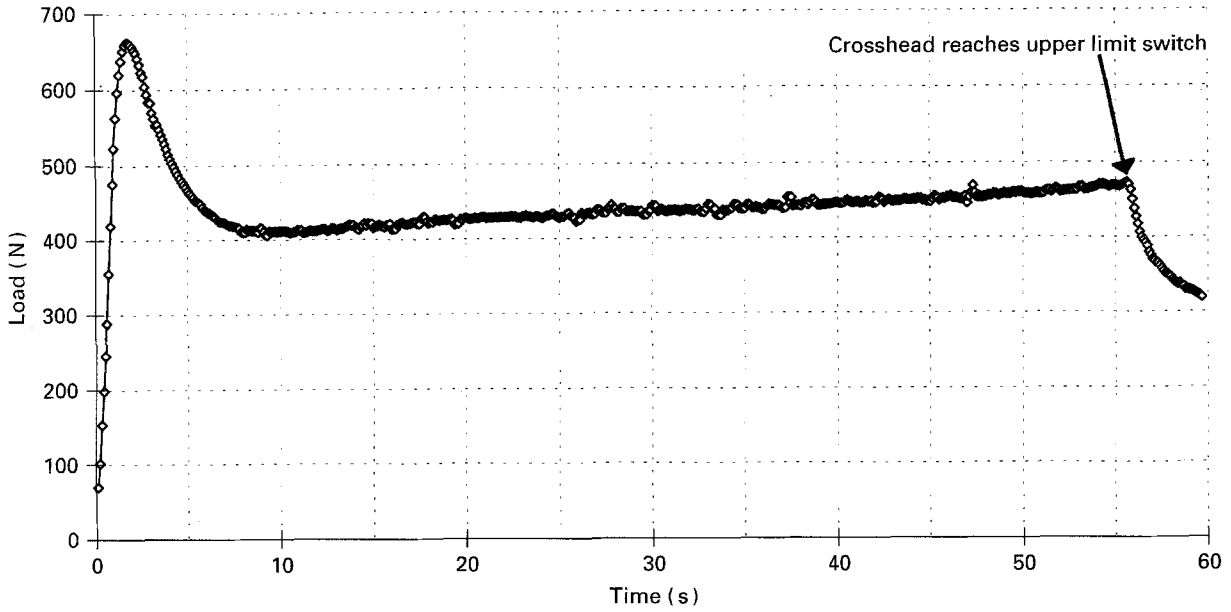

Figure 2 Computer-monitored draw load curve for a necking polymer: GSE16 PP drawn at 200 mm min^{-1} at 110 °C.

work, the locations and relative positions of horizontal grid lines at the centre line of the specimen are of interest, so a technique has been developed to determine the positions of these lines in the images. As the camera does not move during the test in the current equipment configuration, strains can be measured by regarding the relative movement of these lines with reference to an image of the undeformed specimen.

Images are post-processed, i.e. the tensile test is completed before images are analysed. Consequently, in its present form the system cannot be used to control the operation of the tensile testing apparatus. However, state of the art tensometers such as those in the Instron 5500 Series now installed in our laboratories, do have a facility for closed-loop feedback control using strain measurement, and work is in progress in this area.

The user selects the centre of the specimen using cursor keys, and the software extracts the values of the pixels along the chosen line from the image. These raw data give an "intensity profile" which comprises characteristic peaks and troughs representing the variations in light intensity caused by the contrasting specimen and grid lines, as shown in Fig. 4. Finding the locations of the grid-lines in the intensity profile has been achieved by locating the troughs in the profile. If the grid lines are actually brighter than the polymer, and are therefore represented by peaks, the intensity profile is inverted (by subtracting each grey level value from the maximum white level of 255), so that the same minima-finding algorithm may be used. Simple thresholding (where a single grey level value is determined such that all pixels with a lower (darker) value are labelled as grid lines, and all pixels with a higher (lighter) value are labelled as unmarked polymer) frequently failed, so a more adaptive technique was sought. This was due to the reduction in contrast of the grid lines at higher strains, as the grid line paint covers a larger physical area.

Initial attempts at enhancing the contrast of the image using homomorphic filtering and histogram equalization [21] were investigated with little success, until a simple solution was found in the frequency domain, where ideal filtering can be supported by eliminating specific spatial frequency components in the image. By removing the zero-frequency term the intensity waveform may be reduced to a signal that oscillates around the zero level, regardless of the actual brightness of the initial image, and by careful choice of the filtering parameters this technique also allows selective filtering of any high-frequency noise present in the profile. This technique benefits from the speed of the dedicated DT2878 array processor, which performs the fast Fourier transforms. It is then necessary to search for zero crossings in the filtered profile, which represent the bounding edges of the grid-lines. However, problems still occur at higher levels of magnification because the ink lines contain low-frequency components and can be stripped down to zero where small higher frequency changes in the local area spawn false zero-crossings. It was found that it was a much simpler task to reject manually obviously false detections than tune the filter transfer function for optimum performance with each image. The former procedure has been used in the current work, but automation is underway.

In the current work, the threshold crossings have been termed "intersections" as they represent the intersection of the intensity line profile with the zero-level. Two intersections are required to define the edges of a grid-line, and once these are located it is possible to calculate the location of the centre of the line. The detected position of the centre of the grid-line should be desensitized to changes in the ambient lighting because the apparent width of the printed line, which may change under different lighting levels, does not affect the calculation – i.e. the troughs in the intensity profile may get wider or narrower, but their centre

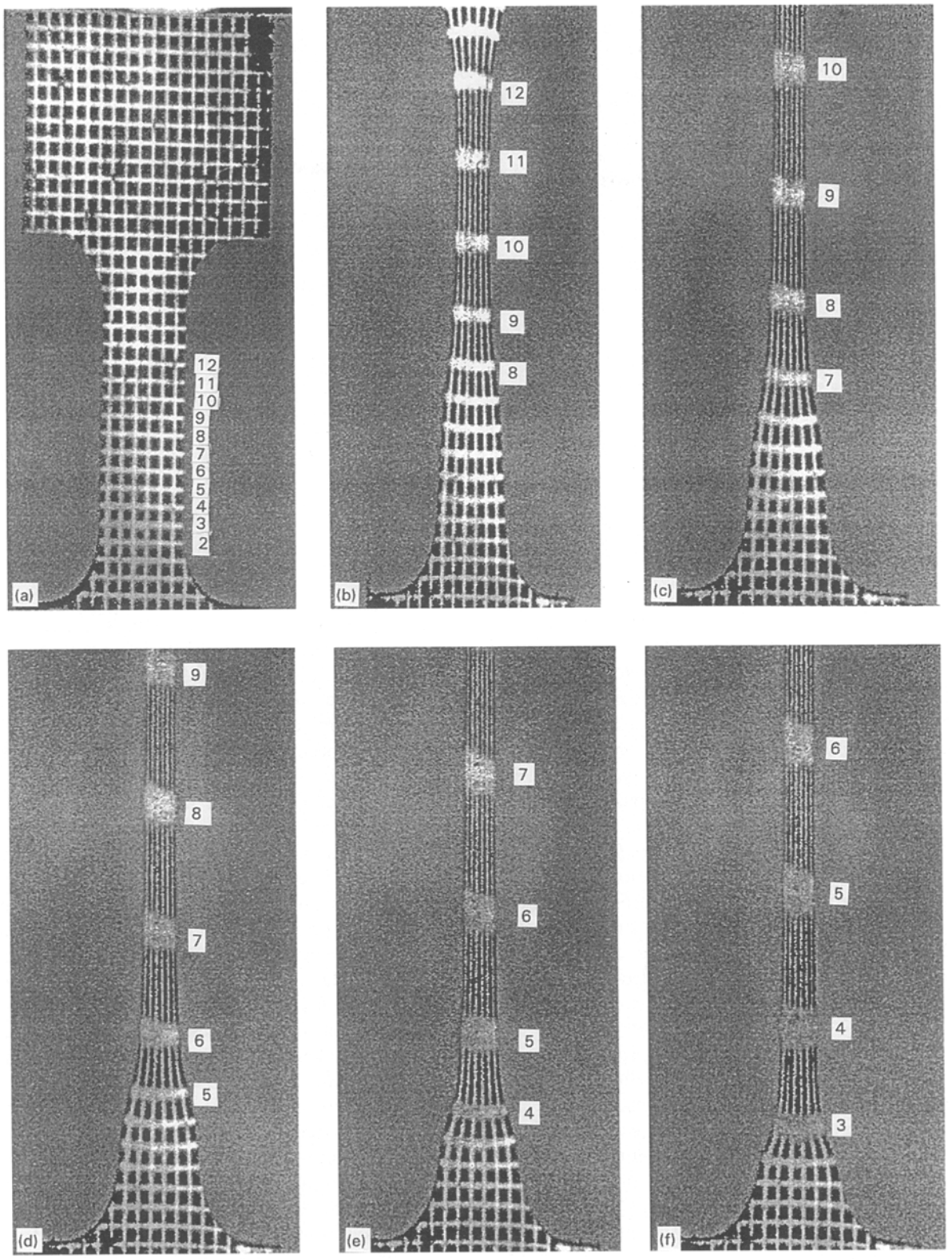

Figure 3 Images of a GSE16 PP drawn uniaxially at 200 mm min^{-1} at 110 °C, at various times during drawing ($t = 0$ is the start of the test). (a) 0 s, (b) 9 s, (c) 18 s, (d) 27 s, (e) 36 s, (f) 45 s.

should not change position. Each grid line in the parallel-sided gauge length is then numbered, starting from the line nearest to the bottom of the image, (nearest to the fixed clamp), then moving upwards through the gauge length towards the moving clamp. The labelling terminology for elements is based on the line-numbering scheme, e.g. el0–1, el1–2, etc., shown in Fig. 3. Note that this labelling technique is image-dependent, and not related to a fixed locus position in the specimen in any way.

Calculating the detected position of a grid line by simply calculating the mid-point between adjacent intersections may not provide a true representation of the location of the grid line in all cases because the intensity distribution of each grid line may not be symmetrical during inhomogeneous drawing. As the

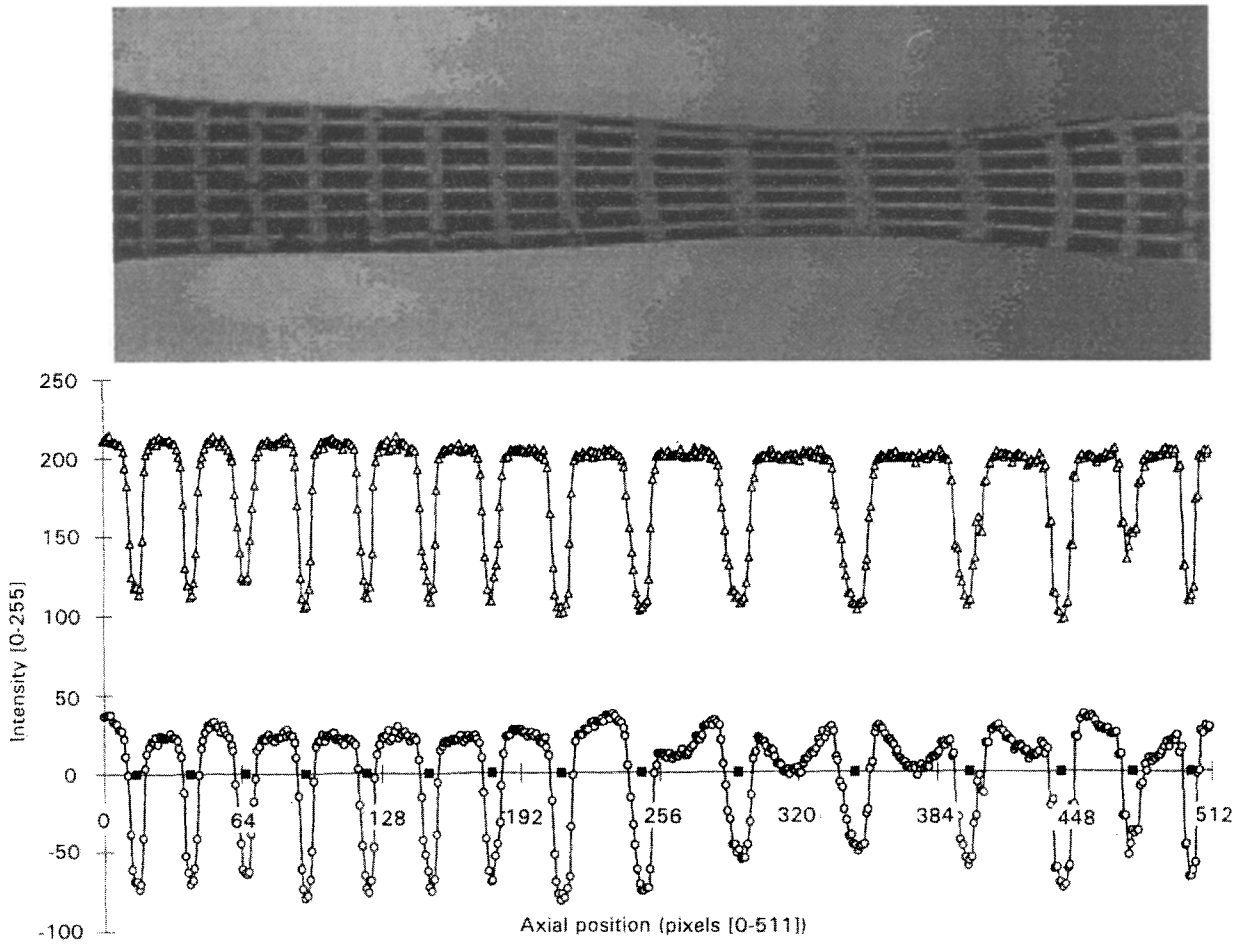

Figure 4 (△) Typical image, line intensity profile and (○) digital Fourier transform (DFT) filtered intensity profile, showing location of grid lines in the image and (■) their detected locations.

neck usually approaches the grid lines from one side, that side of the printed line will be stretched first, resulting in reduced contrast on one side of the line, and consequently the intensity distribution will be asymmetric about the centre of the line. One method of taking this asymmetric intensity distribution into account is to consider the distribution of the grey levels of the pixels making up the grid line, which are those values in the intensity profile between the two axial positions determined as intersections. This can be done by calculating the centroid of such a feature from

$$c = \frac{\sum_{i=\text{start}}^{i=\text{end}} [T - f(i)] \times i}{\sum_{i=\text{start}}^{i=\text{end}} [T - f(i)]} = \frac{\sum_{i=\text{start}}^{i=\text{end}} [if(i)]}{\sum_{i=\text{start}}^{i=\text{end}} [f(i)]} \quad (1)$$

where T is the threshold (and is always zero using the present filter), $f(i)$ is the intensity value at the ith position of the profile, and the two bounding intersections are at profile positions given by start and end values of i.

It is impractical at present to automate the system fully to cater for the varying types of image and levels of strain, because the segmentation algorithms have to cope with highly distorted features at high strains, and would have to be extremely robust. Generally, it has been observed that over-filtering the lower spatial frequencies in the image gives rise to more false detections, but this method is useful for removing low-frequency intensity variations from the image, such as spatial variations in contrast due to uneven lighting and the reduced contrast caused by specimen extension. In the current system, image analysis segmentation results are presented to a human observer for further decision making, providing the user with scope to edit out obviously erroneous results caused by the failure of the segmentation algorithm.

4. Materials

A variety of polymers has been studied using the current image analysis technique, and the results presented here demonstrate the capabilities of the current technique when investigating both the homogeneous drawing exhibited by a carbon-filled styrene butadiene elastomer (Holset Ltd), and the inhomogeneous deformation exhibited by a polypropylene homopolymer (GSE16, originally manufactured by ICI). The elastomer specimens were cut from a sheet of compounded material using a die-cutter with the ASTM-die C geometry, which may be seen in Fig. 5a. Extruded polypropylene sheets, 4.5 mm thick, were CNC milled to produce dumb-bell shaped tensile

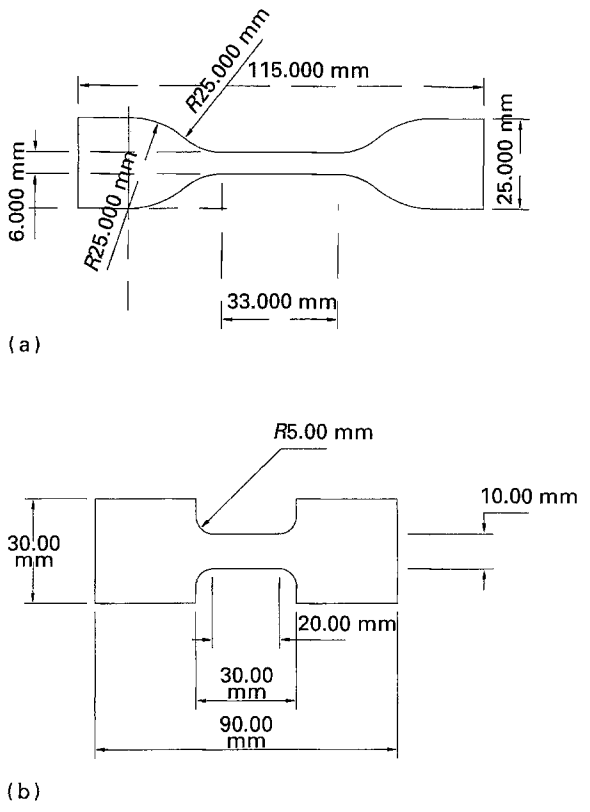

Figure 5 Geometries of specimens used in the current work. (a) ASTM die C geometry used here for elastomers; (b) 20 mm gauge length specimen.

test specimens with a 20 mm parallel-sided gauge length to allow the study of steady-state neck propagation, as shown in Fig. 5b. It was found that in shorter gauge length specimens, the neck reached the shoulders too quickly, whereas the longer gauge length provided more time for neck propagation.

5. Experimental test method

The black elastomer and polypropylene specimens were printed with a contrasting yellow ink using a silk-screen printing process, which was found to be sufficiently rapid and accurate for the current investigation, although alternative marking techniques are being investigated. The screen allows the ink to pass where the coating on the screen has been removed to expose the fine mesh. A Letraset 1/16 in ($\sim$0.16 cm) orthogonal grid was used for the tests reported here. The dimensions of the specimen gauge length were measured prior to printing, to prevent the micrometer faces from damaging the printed grid lines.

To provide data for other research programmes in our laboratories, the elastomer samples were tested at ambient temperature at a crosshead speed of 500 mm min^{-1} [26, 27]. Following earlier work in our laboratories [28, 29], GSE16PP specimens were tested at 110 °C at crosshead speed of 200 mm min^{-1}, where they readily neck and draw. The main aim of this work was not to compare the behaviour of these materials directly, but to demonstrate the applicability and value of the image analysis technique.

When testing at elevated temperatures, an image of the cold specimen was taken prior to heating, to provide a visual calibration before any thermal expansion occurred. Only the top of the specimen was clamped prior to heating to allow the specimen to hang freely, and the temperature was raised to the set point where it was left to equilibrate for around 10 min before the final tightening of the lower clamp. After a further 10 min the test was started, a procedure chosen to allow sufficient time for heating yet reduce any buckling and compressive effects caused by thermal expansion in the gripped specimen.

Image and data capture software is run on the PC, which first prompts the user for basic test details which are saved to file to provide consistent test administration. The user can then configure the software to capture data for the test in hand by choosing both image and load data sampling rates, but data capture does not begin until the electronic trigger is received from the Instron to indicate that the crosshead has started moving. During the test 16 images are captured (including one at time $t = 0$), and the draw load is acquired concurrently, but at a higher sampling rate to provide more detailed load–time data. The draw load curve (as shown in Fig. 2) together with images of the deforming polymer captured during drawing (such as Fig. 3), or from the video recording of the test form the raw data for a single test.

The imaging system provides a non-contacting measure of the surface strains experienced by the specimens, and the total draw force is known from the load cell, but the local true stresses in the specimen cannot be calculated without making assumptions about the nature of the deformation or the distribution of the load within the specimen geometry.

Assuming that deformation occurs at constant volume, the actual cross-sectional area of each element can be calculated from the initial volume of the element, and the surface strains, allowing the true stress to be calculated from the monitored draw load and the measured strains (see Fig. 6). In the current work the axial centre line is used for all measurements, where deformation is predominantly uniaxial. The specimen is essentially regarded as a number of parallel elements in tension, so the load is distributed equally between this number of elements, which remains constant during the deformation process. The calculations are shown in the following sections.

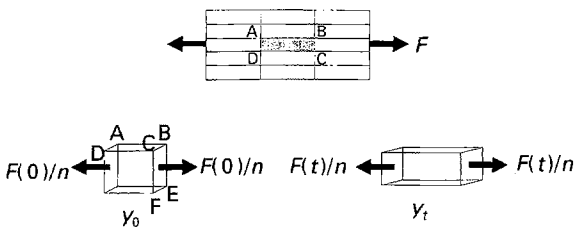

Figure 6 Loading of elements: F is the total time-dependent draw load, assumed to be shared equally by n elements across the gauge length, and used, with axial length y_t, and original element cross-sectional area, BCEF, to obtain elemental stress, strain and strain rate.

5.1. Draw ratio

$$\lambda_t = \frac{y_t}{y_0} \tag{2}$$

where y_t is the current axial length at time t and y_0 is the original axial length measured by image analysis (see Fig. 6). Being a ratio, no conversion to SI units from pixels is necessary.

5.2. Axial strain

$$\begin{aligned}\varepsilon_t &= \int_{y_0}^{y_t} d\varepsilon \\ &= \int_{y_0}^{y_t} \frac{dy}{y} \\ &= \ln\left(\frac{y_t}{y_0}\right) \\ &= \ln(\lambda)\end{aligned} \tag{3}$$

5.3. Axial strain rate

At time t' (the median time between two frames)

$$\dot{\varepsilon}_t' = \left(\frac{\varepsilon_{t+\Delta t} - \varepsilon_t}{\Delta t}\right) \tag{4}$$

This technique allows the generation of true strain-rate data during the inhomogeneous deformation region after yield, where the machine imposed strain rate, $\dot{\varepsilon}_m = V/L$ (V is the crosshead speed and L is the gauge length of the specimen) no longer applies locally.

5.4. True stress

It is first necessary to calculate the original volume, $V_0 = x_0 y_0 Z$ of the deformation element. Each element is defined by the area of the silk-screen printed grid, e.g. the element bounded by ABCD in Fig. 6 where x_0 is BC and y_0 is AB, and passes through the complete thickness of the specimen, so the thickness, Z, of the gauge length must be measured.

Now, at a time, t, the current axial length of the element, y_t, may be used with the constant volume assumption to calculate the actual cross-sectional area $A_t = V_0/y_t$ over which the distributed force acts.

As the load is assumed to be distributed equally between all elements across the width of the gauge length region, the number of elements must be known, requiring the original gauge width of the specimen.

If the original gauge width is W, the number of elements, n, is

$$n = \frac{W}{x_0} \tag{5}$$

The distributed load is therefore $1/n$th of the total draw force, F. The true stress is given by

$$\begin{aligned}\sigma_t &= \frac{F}{A} = \left(\frac{y_t}{x_0 y_0 Z}\right)\left(\frac{F_{\text{tot}}}{W/x_0}\right) \\ &= \frac{F_{\text{tot}} y_t}{y_0 Z W}\end{aligned} \tag{6}$$

but $ZW = A_0$, the original cross-sectional area, consequently

$$\begin{aligned}\sigma_t &= \frac{F_{\text{tot}}}{A_0}\lambda \\ &= \sigma_E \lambda \\ &= \sigma_E(1 + e)\end{aligned} \tag{7}$$

where σ_E is the engineering stress (force/original cross-sectional area). The true stress calculation is independent of the elemental width, but is only valid for the region over which deformation is approximately homogeneous.

The assumption of deformation at constant volume has been used throughout. However, it is possible to calculate the true stress if either the actual change in volume or Poisson's ratio are known as a function of strain. Equation 7 has previously been applied to the deformation of polymers by Meinel and Peterlin [22, 23], amongst others.

6. Results

Data are first presented for the apparently simpler case of homogeneous deformation. However, as a primary aim of our work was to investigate the inhomogeneous deformation of polymer specimens, i.e. necking, fuller data are presented for a GSE16 polypropylene homopolymer, together with typical process true stress–strain curves for this material at a range of constant extension rates. In each case, the image composition was adjusted as necessary to provide the optimum compromise of allowing sufficient extension to generate adequate high-strain results yet making the original grid spacing as large as possible to provide accurate test results. However, as apparently homogeneous deformation is the simplest mode of deformation, these results are presented first. In the following figures, the measured or derived values are joined by straight lines to aid in observing the trend, not to imply an exact relationship.

6.1. Homogeneous deformation

Fig. 7 shows typical true elemental process stress and strain versus time curves for a carbon-filled styrene–butadiene rubber (SBR) drawn at 500 mm min^{-1} and at ambient temperature. The process stress–strain curve obtained by cross-plotting these data can be seen in Fig. 8, where all elements appear to generate very similar values at the same times, indicating that the deformation is homogeneous. During imaging it was observed that as all elements in the specimen gauge length were drawn, elements that were in the field of view at the start of the test quickly moved out, and previously unobservable elements entered the field of the view. This is due to the image composition, which had been chosen to observe just a few elements in the gauge length. A substantial part of the material outside of the gauge length (i.e. in the shoulders of the specimen) could be seen to enter the images during the test, but data

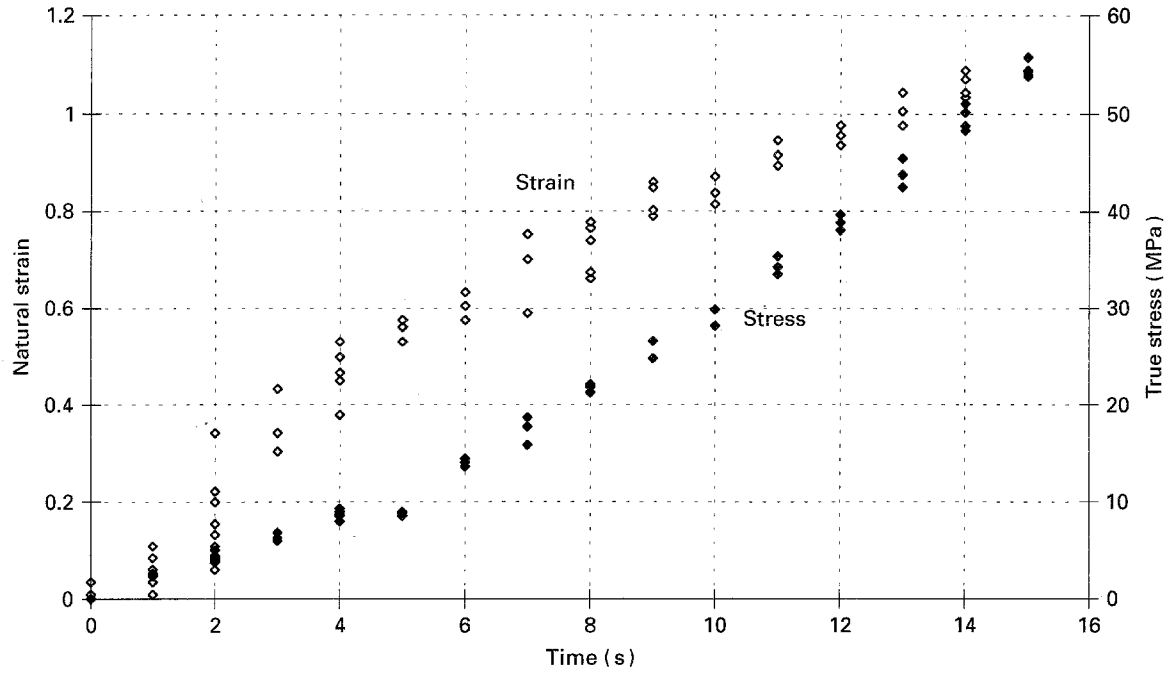

Figure 7 (◆) True stress and (◇) strain versus time curves for a carbon-filled styrene–butadiene rubber (SBR) drawn at 500 mm min^{-1} and at ambient temperature.

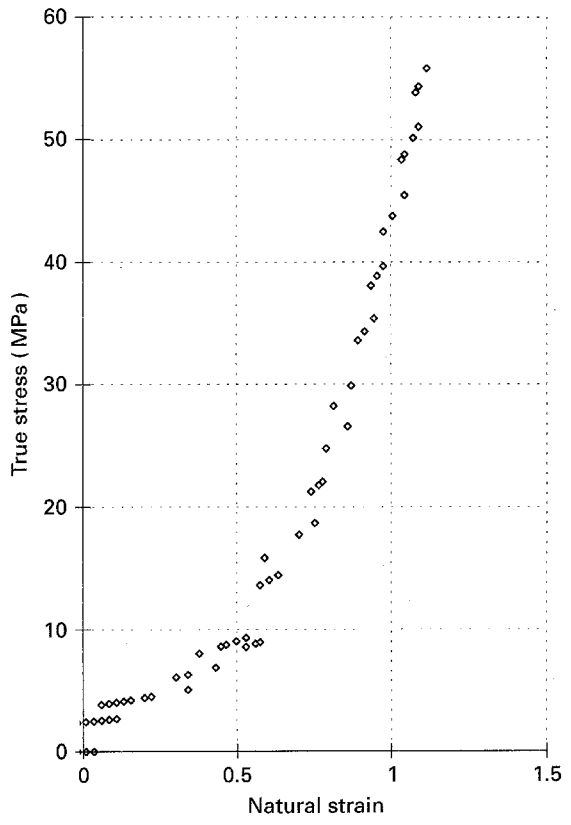

Figure 8 SBR elastomer process true stress versus strain.

generated by these elements have been excluded from the results because the assumptions used in the true stress calculations would no longer be valid for such elements. The results demonstrate the relatively homogeneous deformation nature of this material, all elements undergoing the same deformation process to a good approximation. Localized (i.e. single element) measures of strain are consequently not vital. However, due to the extent of deformation in the shoulders of the specimens, simply using the clamp separation as a direct indicator of strain in the specimen is inaccurate.

6.2. Inhomogeneous deformation – GSE16 polypropylene homopolymer

6.2.1. Neck propagation

Fig. 9 shows the natural strain versus time data for individual elements along the gauge length. The steady-state nature of neck propagation can clearly be seen in that the strain–time profile for each element may be superposed by shifting towards $t = 0$. Each element is taken through the neck in turn, from isotropic pre-neck material to drawn oriented post-neck material. From Fig. 9, it is apparent that the neck was initiated in elements 9–10, 10–11 and 11–12, as these are the first elements to show a rise in strain. The neck then propagated back along the gauge length, taking elements 8–9, 7–8, 6–7 etc. in sequence. At the end of the image sequence (after 45 s drawing), element 2–3 was just entering the neck, whereas elements 0–1 and 1–2 appear to remain undeformed. To see deformation in these elements it would have been necessary to capture images for a longer time period, because drawing continued after the images were acquired and elements 1–2 and 0–1 would be reached by the neck some time later. The resulting drawn product when removed from the tester cannot be compared with the final image acquired during the test unless the final image was captured after the upper clamp had reached its traverse limit. Even then, the elastic recovery of the specimen after the clamps are released is sufficient to ensure that any form of post-test re-calibration would cause uncertainties. The gauge length of these specimens was chosen specifically to allow the investigation

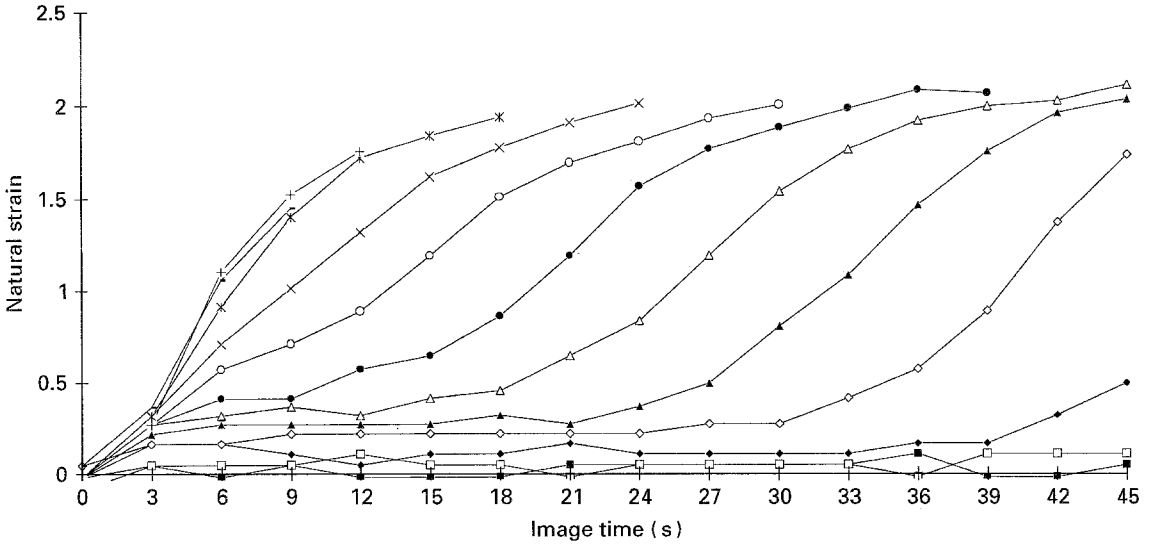

Figure 9 Strain versus time in individual elements along the gauge length, for GSE16 PP drawn uniaxially at 200 mm min^{-1} at 110 °C. Elements: (■) 0–1, (□) 1–2, (◆) 2–3, (◇) 3–4, (▲) 4–5, (△) 5–6, (●) 6–7, (○) 7–8, (×) 8–9, (✳) 9–10, (+) 10–11, (■) 11–12.

of neck propagation, as the neck was found to reach the shoulders rapidly after neck initiation in short gauge length specimens, which allowed fewer images to be taken during the time that the neck was undergoing steady state neck propagation.

The neck propagation velocity can be measured from the horizontal separation of the strain–time curves. For example, at $\varepsilon = 1$, the average interval is 6.7 s. Because the elemental spacing is known from the original grid spacing, (1/16 in $\approx$ 1.59 mm in this case), the neck propagation velocity may be calculated as 0.24 mm s^{-1}. An equation for the neck propagation velocity, v_p, in a uniaxial tensile test has been proposed by Coates and Ward [24]

$$v_p = \frac{V}{(2\lambda_{max} - 1)} \quad (8)$$

where V is the crosshead speed (200 mm min^{-1} in this case), and λ_{max} is the maximum draw ratio achieved through the neck. Using the test speed of 3.33 mm s^{-1}, and the maximum measured draw ratio of 8.55, this gives a calculated neck propagation velocity of 0.22 mm min^{-1}, which compares well with the value 0.24 mm s^{-1} obtained using image analysis.

6.2.2. Strain rates

The elemental strain rates versus time are shown in Fig. 10. There appears to be a much higher strain-rate peak and sharper strain-rate profile (i.e. narrower peak) experienced by elements 10–11 and 11–12 (and to a lesser extent 9–10) than the others. It appears that the neck did not form exactly in the middle of an element (there is no reason to suggest why it should), but formed slightly more in element 10–11, near to the border with 11–12. There is also a sampling rate issue to be raised here, which will be discussed below. Consequently, element 9–10 was further away from the point of neck initiation and does not experience a strain-rate peak as high as in 10–11 and 11–12. Subsequent elements are deformed during the neck-propagation process, again each element taken in turn through the neck. The jagged nature of these curves is an artefact of the method of digital differentiation used to calculate the strain-rate values, which is particularly sensitive to the discrete resolution (quantization) of the measurement.

Fig. 11 shows true axial stress in each element, and it is apparent that elements 9–10, 10–11 and 11–12 exhibit an increasing true axial stress with time, even though the draw load passes through a maximum at the yield point and then falls, whereas elements 0–1 and 1–2 are taken through a local maximum in true stress before a reduction in true stress that follows the shape of the peak in the draw load curve. Limitations introduced by the chosen image sampling frequency are evident because the peak in true axial stress at 3 s does not correspond with the peak in draw load that occurs just prior to this image being taken. As in any digitally sampled time-varying signal, the sample interval required to reproduce the signal faithfully is a function of the maximum frequency of the time-varying signal (the sampling frequency must be at least twice that of the signal being sampled to fulfil the Shannon/Nyquist sampling criterion).

Because the elements outside the neck, but still within the gauge length region are not plastically deformed until they are reached by the neck, their true axial stress is sensitive to the changes in the draw load – their cross-sectional area remaining almost constant. The neck reaches these elements after the initial load peak during the draw load "plateau", so their area changes during the period of the draw load plateau. (However, in many cases the draw load has also been seen to be rising slightly during neck propagation, so cannot correctly be described as constant, but for simplicity in this discussion can be regarded as changing much less rapidly with time than during the initial loading and yield.) The complete true stress process history for these elements is initially sensitive to the load transition then, after a certain time related to

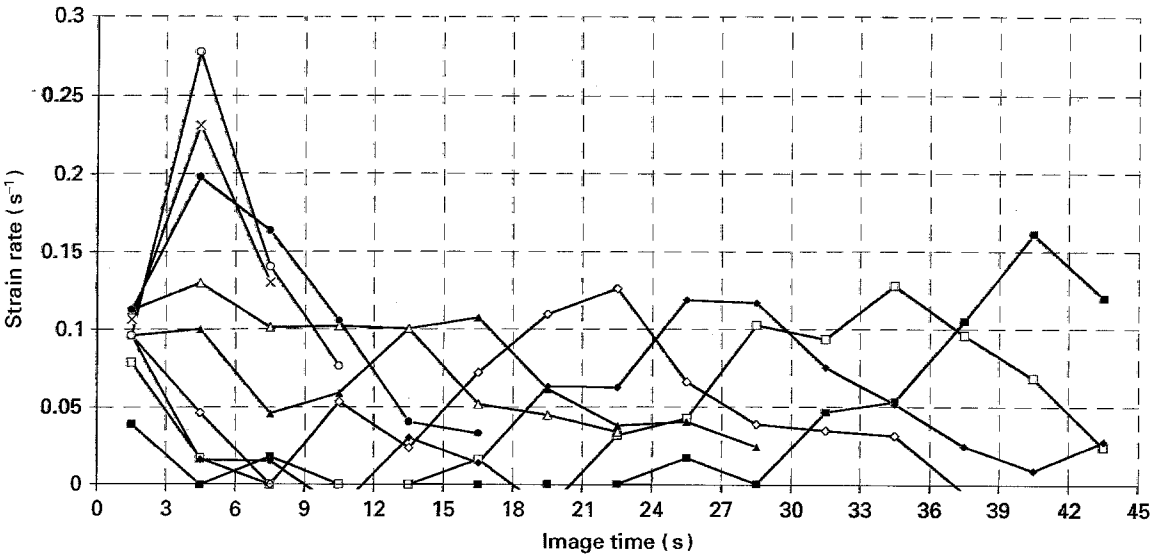

Figure 10 Strain rate versus time for individual elements along the gauge length for GSE16 PP drawn uniaxially at 200 mm min^{-1} at 110 °C. Elements: (■) 3–4, (□) 4–5, (◆) 5–6, (◇) 6–7, (▲) 7–8, (△) 8–9, (●) 9–10, (○) 10–11, (×) 11–12.

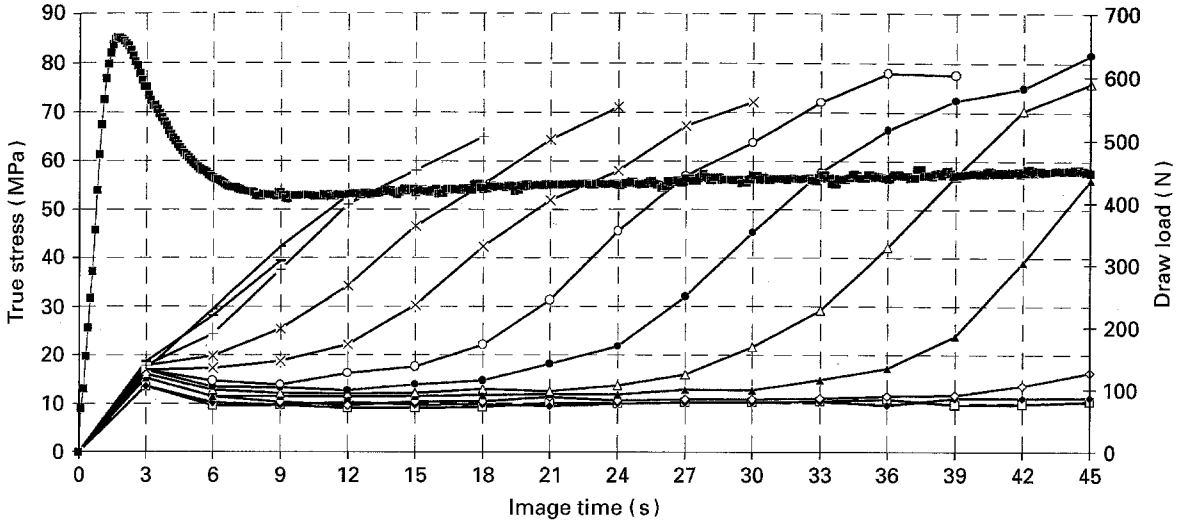

Figure 11 True stress versus time for individual elements along the gauge length, with (■) draw load superimposed, for GSE16 PP drawn uniaxially at 200 mm min^{-1} at 110° C. Elements: (□) 0–1, (◆) 1–2, (◇) 2–3, (▲) 3–4, (△) 4–5, (●) 5–6, (○) 6–7, (×) 7–8, (✳) 8–9, (+) 9–10, (—) 10–11, (-) 11–12.

their position from the point of neck initiation, their stress is derived primarily from their changes in strain.

6.2.3. Process true stress–strain curves

Knowing the true axial stress and natural axial strain for each element at a given time makes it possible to generate the true process stress–strain curve by cross-plotting these data, which can be seen in Fig. 12. An important feature in this figure is the group of isolated points lying above the main curve at low strains, which although they appear erroneous, are actually related to the peak in the draw load at yield, which will be discussed in fuller detail in a separate publication, focusing on neck initiation. The process true stress–strain data have also been used as input to finite element analysis models to predict the deformation behaviour of tensile specimens – the preliminary results have been presented elsewhere [20, 30, 31].

The strain rate varies through the process, and may also be plotted as a function of draw ratio, demonstrating that as the material is taken along through the deformation process, the strain-rate is low for the isotropic material, then rises through a maximum as the material passes through the neck, and falls back to a low value as the post-neck material work hardens and resists further deformation, as shown in Fig. 13. This strain-rate versus draw ratio peak may be regarded as an indication of neck "sharpness" [24]. When interpreting Fig. 13 it must be remembered that the points cannot be averaged to form a smooth peak, because each data series represents data for different elements which undergo different deformation processes related to their position in the specimen with respect to the point of neck initiation.

Those elements which are in the neck as it forms experience their initial straining under higher draw load, and hence lie higher than the global curve (made

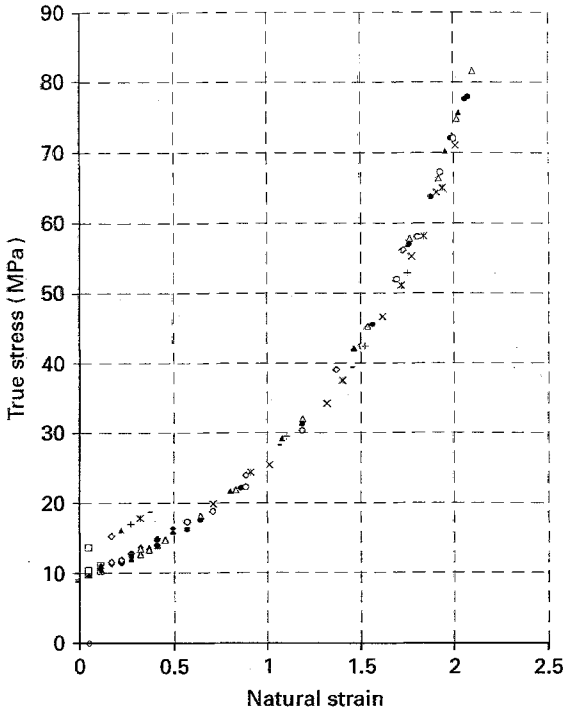

Figure 12 Process true stress versus natural strain curves constructed from individual element stress-strain curve, for GSE16 PP drawn uniaxially at 200 mm min^{-1} at 110 °C. Elements: (■) 0–1, (□) 1–2, (◆) 2–3, (◇) 3–4, (▲) 4–5, (△) 5–6, (●) 6–7, (○) 7–8, (×) 8–9, (✳) 9–10, (+) 10–11, (-) 11–12.

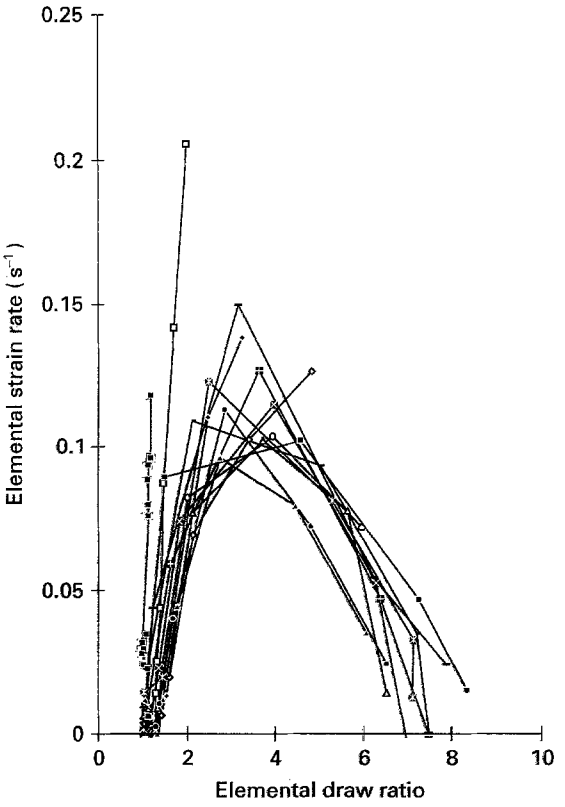

Figure 13 Strain rate versus draw ratio response, constructed from individual element strain rate–strain curves for GSE16 PP drawn uniaxially at 200 mm min^{-1} at 110° C. Elements: (■) 1.5 s, (□) 4.5 s, (◆) 7.5 s, (◇) 10.5 s, (▲) 13.5 s, (△) 16.5 s, (●) 19.5 s, (○) 22.5 s, (⊠) 28.5 s, (⊠) 31.5 s, (▦) 34.5 s, (-) 37.5 s, (—) 40.5 s, (▣) 43.5 s.

up of elements which lay outside the neck as it forms, but still within the gauge length). The stress in these elements is sensitive to changes in both load and area making their behaviour more difficult to interpret, but the experimental results indicate that the area must be decreasing at a faster rate than the load is decreasing after yield, thereby maintaining an increasing true stress within these elements during the fall in load.

6.2.4. Influence of crosshead speed on the process true stress–strain data

Fig. 14 shows three process true stress–strain curves for samples of GSE16 PP drawn at 110° C. As expected, increasing the crosshead speed raises the stresses generated during the test. It is also evident that the strain achieved through the neck is also increased for higher crosshead speeds, which may be due to thermal effects when drawing at higher speeds (see Table I).

It has been suggested that there exists a three-dimensional isothermal stress–strain–strain-rate surface for uniaxial extension of polymers [4, 32], but although these results allow the generation of stress, strain and strain-rate triplets, and the process true stress–strain curve presented traces a path across this surface, it is still not possible to generate the three-dimensional surface. This is because the single-stage tensile test only covers a small range of strain rates at the higher strains, the range being fixed by the crosshead speed of the test. Away from the neck, nearly all of the material in tensile test specimens deforms at very low rates of strain, so the material is at low strain rates at both low strain and high-strain – the peak in strain rate is not at the highest strain, but in the neck.

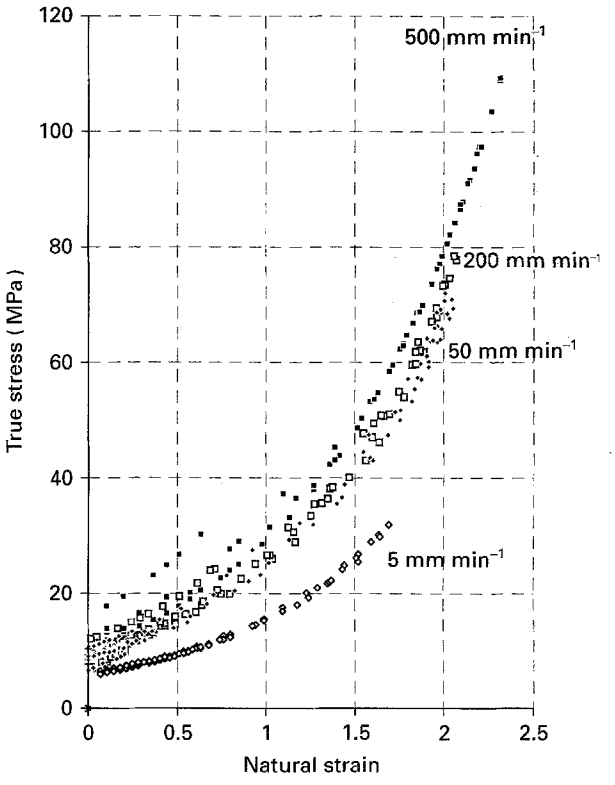

Figure 14 Process true stress–strain curves for GSE16 PP drawn at 110 °C, at crosshead speeds of 5, 50, 200 and 500 mm min^{-1}.

The current technique allows the determination of the true stress–strain and strain-rate data for individual material elements before, during and after the neck, allowing detailed investigations of the deformation

TABLE I Measured and calculated neck propagation velocities

Crosshead speed (mm min^{-1})	Measured λ_{max}	Measured neck speed (mm s^{-1})	Predicted neck speed (mm s^{-1})
5	5.6	0.0091	0.0091
50	7.2	0.069	0.067
200	8.55	0.24	0.22
500	10.11	0.35	0.46

behaviour of materials at high strains, such as those experienced in die-drawing and geogrids. Fuller stress–strain–strain-rate data could clearly be obtained from redrawing of post-neck material; such work is part of an on-going study.

Testing at a range of crosshead speeds also allows further comparison of the neck-propagation velocities measured and predicted by the Coates and Ward equation. It is clear that good agreement is obtained at speeds up to 200 mm min^{-1}, but there is some deviation at higher speeds which may be due to thermal effects.

6.2.5. Extensional viscosity

The apparent extensional viscosity, which represents the resistance to extensional deformation during drawing, may be calculated from the ratio of axial stress to axial strain rate. The image analysis technique presented here allows determination of these quantities for each element in the field of view, providing an assessment of apparent extensional viscosity as a function of axial strain (because the strain state of each element is known), or axial strain rate. As in the case of the stress–strain–strain-rate surface, however, only limited information can be obtained, because data are not obtained at constant axial strain rate: a full extensional viscosity–strain–strain-rate surface cannot be generated from these experiments, unless extensive tests, involving redrawing of post-neck material, can be undertaken. Even so, it is illuminating to obtain extensional viscosity–strain relationships for the actual specimens undergoing necking. Fig. 15 shows a typical plot of apparent extensional viscosity versus axial strain for several elements for the PP GSE16 specimen whose base data are presented in Figs 9–11. Although strain-rate determination (and hence extensional viscosity) is subject to larger errors than stress or strain measurement, certain features of the curve are notable.

At very low strains, the apparent extensional viscosity appears to be falling with increasing draw ratio, i.e. the resistance to deformation appears to be decreasing. This might be associated with the commencement of break down of spherulitic morphology at low draw ratios. Care must be taken in interpretation here, as the fall in apparent extensional viscosity may also be due to strain rate increasing rapidly (and more rapidly than stress) as low draw-ratio elements enter the neck (see Fig. 13), or, more plausibly, to a combination of strain rate and morphological effects. It is not possible to separate out the effects of these two factors from the present experiments. As draw ratio continues to increase, the apparent extensional viscosity becomes relatively steady, possibly increasing slightly with draw ratio, at a low value. This may be tentatively interpreted as continuing re-ordering of the polymer morphology by spherulitic distortion towards a fibrillar structure occurring at relatively constant resistance to deformation, with elements passing through the peak strain rates in the neck by draw ratio 3 or 4. As the draw ratio reaches values around 6 the fibrillar structure will prevail, and drawing involves crystalline orientation in a fibrillar structure, with increasing crystal continuity being developed; under these conditions, significant strain-hardening behaviour is observed, and the fall in strain rate with strain is reflected in the rapid increase in apparent viscosity. This latter rise, related to strain hardening is perhaps the most readily understood feature of Fig. 15. It is tempting to ascribe the low draw-ratio fall to a strain-softening mechanism, but this cannot be defended from the available data.

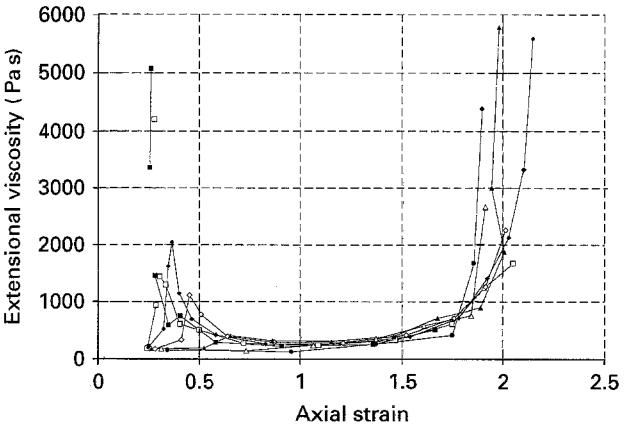

Figure 15 Apparent extensional viscosity versus draw ratio for GSE16PP drawn uniaxially at 200 mm min^{-1} at 110° C. Elements: (■) 5–6, (□) 6–7, (◆) 7–8, (◇) 8–9, (▲) 9–10, (△) 10–11, (●) 11–12.

6.3. Measurement errors

In any measurement technique it is important to assess the source of errors. In the current measurement technique, the precision of the strain measurement is dependent on the resolution of the imaging system, and the precision of the load measurement is dependent on the resolution of the load-cell and analogue to digital conversion. The measurement resolution is limited to $\pm$ 1 pixel, but expressing this as 0.2% (1/512) is misleading because this does not take into account the actual feature length in the image, and the fact that there are errors associated with locating each edge of the feature. For example, if each element is approximately 25 pixels wide, then the error in measurement is at worst 4% (two lines are required to define a grid element), and the error in locating each grid line will be 0.2%, producing a combined error of (2/25 pixels $\times$ 1 mm) = 0.08 mm which is equivalent to a measurement accuracy of 0.8% relative to a gauge length of 10 mm. If this feature is 1 mm long, 4% constitutes a measurement error of 0.04 mm, which equates to a percentage error of 0.4% relative to a gauge length of 10 mm. Also, as the specimen

deforms, the feature length increases, so the errors associated in measurement may decrease. Unfortunately, the feature lines themselves become more difficult to detect as the grid line paint becomes spread over a wider area, and its contrast is therefore reduced. Consequently, it is difficult to make exact statements of the accuracy of this technique, and comparing the measurements with manual measurement techniques is not a practical or conclusive exercise because any human perception of where the centre of a printed grid line is will always be subjective.

7. Conclusions

1. It has been shown that image analysis can be used to determine the true stress–strain–strain-rate behaviour of polymers. An image analysis system has been implemented which allows accurate monitoring of the surface strain distribution in deforming materials to a limiting resolution of 0.2% of the resolution of the image (1 pixel in 512), by measurement of printed grid displacements. The current system has provided a semi-automated route to the rapid and accurate determination of true process stress–strain and strain-rate information.

2. The system has been applied successfully to both homogeneous and inhomogeneous modes of tensile deformation and is, in principle, also suitable for biaxial deformation.

3. The ability to capture images at accurately timed intervals has enabled the determination of true strain-rates for local elements during the non-homogeneous deformation of a polypropylene.

4. The success of automatic image analysis is limited at high strains by the deformation of the features of interest (the horizontal grid lines), making it necessary for more user involvement in the analysis of images at higher strains. Analysis is further complicated by the vertical grid lines which move closer together at high strains, making it difficult to pick a vertical intensity line profile which does not intercept the vertical grid lines, so causing erroneous results. In general, the silk-screen printing process has been found to be an adequate method for the rapid marking of the specimens, provided that a suitable ink is found which does not crack and flake-off the specimen during deformation at elevated temperatures.

5. Accurate synchronization of the load data to the images was found to be critical for the accurate determination of true stress to be calculated, both during live image capture and when re-analysing pre-recorded video recordings of the test.

6. A time series of strain measurements made during neck propagation has supported the concept of neck propagation at constant velocity. Measured values of neck-propagation velocity agree well with predicted values.

7. Process true stress–strain curves demonstrate that although the deformation of polymer specimens is inhomogeneous, the individual contributions of the deformation experienced by each element can be isolated from the macroscopic deformation displayed by the specimen as a whole.

Acknowledgements

The authors thank SERC and IBM (UK) Laboratories for the CASE studentship awarded to A.R.H. Personal thanks are due to Dr Colin Bird, IBM UK Scientific Centre and Dr Neil Kirby, IBM Laboratories, and also to Mr Mark Fellows for sample preparation.

References

1. A. J. WILLS, G. CAPACCIO and I. M. WARD, *J. Polym. Sci. Polymer Phys. Ed.* **18** (1980) 493.
2. M. A. WILDING and I. M. WARD, *Polymer* **22** (1981) 870.
3. D. L. M. CANSFIELD, G. CAPACCIO and I. M. WARD, *Polym. Eng. Sci.* **16** (1976) 721.
4. P. D. COATES and I. M. WARD, *J. Mater. Sci.* **13** (1978) 1957.
5. D. I. WIMPENNY, *Mater. Design* **13**(1) (1992) 29.
6. N. E. WRIGLEY, *Mater. Sci. Technol.* **3** (1987) 161.
7. F. J. LOCKETT, *Mater. Design* **13**(2) (1992) 71.
8. R. N. HAWARD, *Polymer* **28** (1987) 1485.
9. C. G'SELL and J. J. JONAS, *J. Mater. Sci.* **14** (1979) 583.
10. C. G'SELL, J. M. HIVER, A. DAHOUN and A. SOUAHI, *ibid.* **27** (1992) 5031.
11. J. S. SIRKIS and T. J. LIM, *Exp. Mech.* December (1991) 382.
12. D. N. HARVEY, Proceedings IDDRG 13th Biennial Congress, February 20 1984, Melbourne, Australia, p. 403.
13. S. M. METWALLI, A. R. RAGAB, A.H. KAMEL and A. A. SAHAB, IBM Kuwait Scientific Centre Report - KSC013, July 1985.
14. A. R. RAGAB, S. M. METWALLI and J. RUEDA, "Current advances in Mechanical Design and Production", Third Cairo University MDP Conference, Cairo, 28–30 December 1985 (Pergamon Press).
15. S. M. METWALLI, A. R. RAGAB, A. H. KAMEL and A. ABDUL SAHEB, *Exp. Mech.* December (1987) 414.
16. V. J. PARKS, *Opt. Eng.* **21** (1982) 633.
17. J. S. SIRKIS and C. E. TAYLOR, *Exp. Mech.* **30** (1990) 26.
18. J. S. SIRKIS, *Opt. Eng.* **29** (1990) 1485.
19. A. R. HAYNES and P. D. COATES, in "Proceedings of the Polymer Processing Society 9th Annual Meeting", Manchester, UK (Polymer Processing Society; 1992) p. 418.
20. P. D. COATES, R. G. SPEIGHT and A. R. HAYNES, *Polymer* **35** (1994) 3831.
21. A. R. HAYNES, PhD thesis, University of Bradford (1994).
22. A. PETERLIN, *J. Mater. Sci.* **6** (1971) 490.
23. G. MEINEL and A. PETERLIN, *J. Polym. Sci.* (*A*-2) **9** (1971) 67.
24. P. D. COATES and I. M. WARD, *J. Mater. Sci.* **15** (1980) 2897.
25. S. NAZARENKO, S. BENSASON, A. HILTNER and E. BAER, *Polymer* **35** (1994) 3883.
26. J. M. ALLPORT, PhD thesis, University of Bradford (1994).
27. V. NOPARATANAKAILAS, PhD thesis, University of Bradford (1994).
28. S. M. POURMAHNAEI, PhD thesis, University of Bradford (1989).
29. P. D. COATES, D. I. ELLIS and S. M. POURMAHNAEI, *Plast. Rubb. Process. Applic.* **8** (1987) 165.
30. A. J. DAY, J. M. ALLPORT, W. P. FISCHER, P. D. COATES and A. MIMAROGLU, in "Proceedings of the ABAQUS Users Conference", Aachen (HKS, Rhode Island, 1993) pp. 151–64.
31. A. R. HAYNES and P. D. COATES, in "Proceedings of the Polymer Processing Society, Regional Meeting, Strasbourg (Polymer Processing Society, 1994) p. 152.
32. P. D. COATES, PhD thesis, Department of Physics, University of Leeds (1976).

Received 26 June
and accepted 8 September 1995